The Astrophysical Journal Letters, 908:L6 (11pp), 2021 February 10 https://doi.org/10.3847/2041-8213/abdbaf

Cosmic Distances Calibrated to 1% Precision with Gaia EDR3 Parallaxes and Hubble Space Telescope Photometry of 75 Milky Way Cepheids Confirm Tension with ΛCDM

Adam G. Riess[1,2], Stefano Casertano[1], Wenlong Yuan[2], J. Bradley Bowers[2], Lucas Macri[3], Joel C. Zinn[4,6], and Dan Scolnic[5]
[1] Space Telescope Science Institute, 3700 San Martin Drive, Baltimore, MD 21218, USA; ariess@stsci.edu
[2] Department of Physics and Astronomy, Johns Hopkins University, Baltimore, MD 21218, USA
[3] Mitchell Institute for Fundamental Physics & Astronomy, Department of Physics & Astronomy, Texas A&M University, College Station, TX 77843, USA
[4] Department of Astrophysics, American Museum of Natural History, Central Park West at 79th Street, New York, NY 10024, USA
[5] Department of Physics, Duke University, Durham, NC 27708, USA
Received 2020 December 15; revised 2021 January 5; accepted 2021 January 14; published 2021 February 9

Abstract

We present an expanded sample of 75 Milky Way Cepheids with Hubble Space Telescope (HST) photometry and Gaia EDR3 parallaxes, which we use to recalibrate the extragalactic distance ladder and refine the determination of the Hubble constant. All HST observations were obtained with the same instrument (WFC3) and filters (F555W, F814W, F160W) used for imaging of extragalactic Cepheids in Type Ia supernova (SN Ia) hosts. The HST observations used the WFC3 spatial scanning mode to mitigate saturation and reduce pixel-to-pixel calibration errors, reaching a mean photometric error of 5 millimags per observation. We use new Gaia EDR3 parallaxes, greatly improved since DR2, and the period–luminosity (P–L) relation of these Cepheids to simultaneously calibrate the extragalactic distance ladder and to refine the determination of the Gaia EDR3 parallax offset. The resulting geometric calibration of Cepheid luminosities has 1.0% precision, better than any alternative geometric anchor. Applied to the calibration of SNe Ia, it results in a measurement of the Hubble constant of 73.0 ± 1.4 km s^{-1} Mpc^{-1}, in good agreement with conclusions based on earlier Gaia data releases. We also find the slope of the Cepheid P–L relation in the Milky Way, and the metallicity dependence of its zero-point, to be in good agreement with the mean values derived from other galaxies. In combination with the best complementary sources of Cepheid calibration, we reach 1.8% precision and find $H_0 = 73.2 \pm 1.3$ km s^{-1} Mpc^{-1}, a 4.2σ difference with the prediction from Planck CMB observations under ΛCDM. We expect to reach ∼1.3% precision in the near term from an expanded sample of ∼40 SNe Ia in Cepheid hosts.

Unified Astronomy Thesaurus concepts: Hubble constant (758); Annual parallax (42); Cepheid distance (217)

1. Introduction

This is the second paper in a series reporting on efforts to improve knowledge of the distance scale and the Hubble constant (H_0) by combining parallax measurements of Milky Way (MW) Cepheids from the ESA Gaia mission (Gaia Collaboration et al. 2016a, 2016b, 2018) and multiband photometry of these variables from the Hubble Space Telescope (HST). This combination offers the only means at present to provide a ∼1% calibration of the Extragalactic Distance Scale. Neither facility can achieve this ambitious goal alone. Reaching this milestone requires simultaneously measuring Cepheid mean parallaxes to ∼5 μas precision from Gaia and measuring the mean brightness of the same objects to ∼0.01 mag precision with HST on the same photometric systems used to measure their extragalactic counterparts. By using such purely differential flux measurements of Cepheids along the distance ladder, it is possible to circumvent systematic uncertainties related to zero-points and transmission functions, which otherwise incur a systematic uncertainty of ∼2%–3% in the determination of H_0, nearly twice the target goal, even before considering any additional statistical and systematic uncertainties along the distance ladder.

We started building this photometric bridge in 2012, by observing 50 MW Cepheid "Standards," randomly chosen by the HST scheduling process among the 70 known Cepheids with periods of $P > 8$ days, H-band extinction of $A_H < 0.4$ mag and $V > 6$ mag that were targeted in our HST Cycle 20 SNAP program. These selection criteria were adopted to collect the most useful sample for calibration of thousands of extragalactic Cepheids observed in the hosts of 19 Type Ia supernovae (SNe Ia) and the megamaser host NGC 4258. For all 50 Cepheids, we have published (Riess et al. 2018a, 2018b, hereafter R18a, b) near-infrared (NIR) photometry collected with HST/WFC3-IR in F160W (similar to the H band) to reduce systematics caused by reddening and metallicity, and optical photometry obtained with HST/WFC3-UVIS and/or ACS in F555W and F814W (similar to the V and I bands). Observations in these three filters can be combined to form a reddening-free distance measure (Hoffmann et al. 2016; Riess et al. 2016, hereafter R16).

Observing MW Cepheids, which are 15–20 astronomical magnitudes brighter than their extragalactic counterparts, requires extremely brief and precisely known exposure times to mitigate saturation and provide accurate photometry. We accomplished this (R18a, b) through very fast spatial scans with HST, moving the telescope during the observation so that the target covers a long, nearly vertical line over the detector. We used a scan speed of $7\farcs5$ s^{-1}, corresponding to an effective exposure time of 5 ms in the visible and 20 ms in the infrared, much shorter than the minimum effective exposure times possible with the WFC3 hardware.

[6] NSF Astronomy and Astrophysics Postdoctoral Fellow.

Scanning observations are also free from the variations and uncertainties in shutter flight time (for F555W and F814W with WFC3-UVIS) that affect very short pointed observations (Sahu et al. 2015). Spatial scans offer the additional advantage of varying the position of the source on the detector, which averages down pixel-to-pixel errors in the flat fields, and can also be used to vary the pixel phase, reducing the uncertainty from undersampled point-spread-function photometry. Finally, unlike ground-based photometry, which relies on calibrators in the same region of the sky, HST can measure the photometry of MW Cepheids over the whole sky, without concern about regional variations in calibrators. The original sample of 50 should have been sufficient to produce a ∼1% precise calibration of the Cepheid P–L relation (often referred to as the Leavitt Law) in the absence of unexpected systematics in the Gaia parallaxes.

Unfortunately, after launch Gaia was found to suffer from a large thermal oscillation, which produces a variation in the angle between its two fields of view and limits its ability to determine absolute parallaxes from relative astrometry measured at multiple parallax phases. The result is that Gaia parallaxes are affected by an additive error, the so-called "parallax zero-point," clearly identified in Data Release 2 (Gaia Collaboration et al. 2018, DR2) using quasars (Lindegren et al. 2018, hereafter L18). L18 attempted to characterize this error, but—possibly because the solution relies on a still imperfect focal plane calibration (see Figure 16 in L18)—the additive term has been found to vary with the color and/or magnitude of the source and its location on the sky; for this reason, we refer to this term as "parallax offset," rather than zero-point, as it is not a single value. Recognizing this, the Gaia team recommended that users calibrate the offset applicable for their targets from sources with similar color and magnitude. Regrettably, quasars are much bluer and 5–10 mag fainter than MW Cepheids, making them unsuitable as offset calibrators. Riess et al. (2018b) showed that the parallax offset could be measured directly from the Cepheids, but at a high cost in precision, increasing the uncertainty in H_0 by a factor of 2.5—from 1.3% to 3.3%. This lesser precision was sufficient to confirm the present "H_0 tension," but is woefully short of what is possible with fully offset-calibrated Gaia parallaxes. However, with the Gaia offset issue now fully recognized, HST observations of additional MW Cepheids could be designed to help calibrate it.

Thus we began a new program in HST Cycle 27 (GO-15879) designed to better self-calibrate the parallax offset uncertainty by observing MW Cepheids with photometrically predicted parallaxes $\pi > 0.8$ mas. Two free parameters, one additive (i.e., the uncertain parallax offset), the other multiplicative (the Cepheid magnitude scale, corresponding to a constant offset in distance modulus) will effect small and large parallaxes differently so the combination of the new large-parallax sample with the prior smaller-parallax sample will better distinguish these parameters. The program resulted in HST photometry of 25 additional Cepheids; for these, and for our previous 50 Cepheids, we can now use the recently released Gaia EDR3 parallaxes (Gaia Collaboration et al. 2020).

The rest of the paper is organized as follows. In Section 2 we present the three-filter spatial-scan photometry of the 25 new large-parallax MW Cepheids, together with the previously observed 50, for a total sample of 75 Cepheids with HST photometry, and compare them to ground-based measurements in corresponding passbands. In Section 3 we carry out an analysis of the recently released Gaia EDR3 parallaxes for all targets; using the precise and accurate HST photometry to recalibrate the extragalactic distance ladder and refine the measurement of the Hubble constant in Section 4.

2. Additional Milky Way Cepheid Standards

R18a, b described the steps used to measure the photometry of bright MW Cepheids from their rapid spatial scans and comparison to ground-based results in similar passbands; we direct interested readers to those publications for details. Photometric measurement uncertainties at a given phase are less than 0.01 mag. R18b compared phase-corrected observations of individual Cepheids across multiple epochs and found average uncertainties in the resulting light-curve mean magnitudes of 0.021, 0.018, and 0.015 mag in F555W, F814W, and F160W, respectively, with the dominant term being a typical ∼0.02 mag uncertainty in the phase correction to mean light of an individual measurement.

The only changes for this new higher-parallax set of measurements is a 4% increase in requested scan speed, to $7\farcs8\ s^{-1}$, the highest speed available, and the addition of a narrowband filter with the same effective wavelength as F160W, F153M, to check the reliability of photometry for the brightest Cepheids. We found a zero-point difference F160W − F153M for the Cepheids of 1.51 mag, in good agreement with the 1.49 mag difference expected from the STScI calibration and with no significant trend in the difference as a function of flux across 2.5 mag (0.0036 ± 0.0037 mag per mag). Phase corrections to mean light are calculated following the procedures outlined in R18a, b, utilizing exclusively *V*- and *I*-band light curves from the same literature sources given in Table 2 of R18b, listed again in the Appendix. Anderson & Riess (2018) estimate that the effect of wide binaries on the photometric calibration of Cepheids is negligible due to the dominance of Cepheids over their companions in flux but will be addressed for any possible astrometric impact on parallaxes in the next section.

For distance measurements and the determination of H_0, it is useful to combine the three aforementioned bands into the same reddening-free Wesenheit index (Madore 1982) used by R16 for extragalactic Cepheids in the hosts of SNe Ia:

$$m_H^W = m_{F160W} - 0.386(m_{F555W} - m_{F814W}). \quad (1)$$

The reddening ratio of 0.386 is derived from the Fitzpatrick (1999) reddening law with $_V = 3.3$. A difference in R_V of ± 1, valid over a wide range of environments, changes this ratio by less than ± 0.05, but for consistency we use the same value as in R16.

It is useful to compare the HST-system photometry to similar measurements from the ground as done in R18b to test for consistency and to derive useful transformations. For this comparison we make use of the extensive ground-based Cepheid catalog from Groenewegen (2018) with *V*, *J*, *H* photometry and compare these to the full set of HST Cepheids. We first transform the NIR magnitudes derived from various ground systems (e.g., SAAO, BIRCAM, and CIT) as given in the table of Groenewegen (2018) to the 2MASS system following the color transformations given in Breuval et al. (2020). These transformations have a mean of 0.01–0.02 mag. We then apply the transformations between the HST and ground systems given below and compare the two in Figure 1. We note the Cepheid CR-Car is not included in the ground-based catalog. The overall agreement is good, as expected since these transformations were derived from a comparison of the

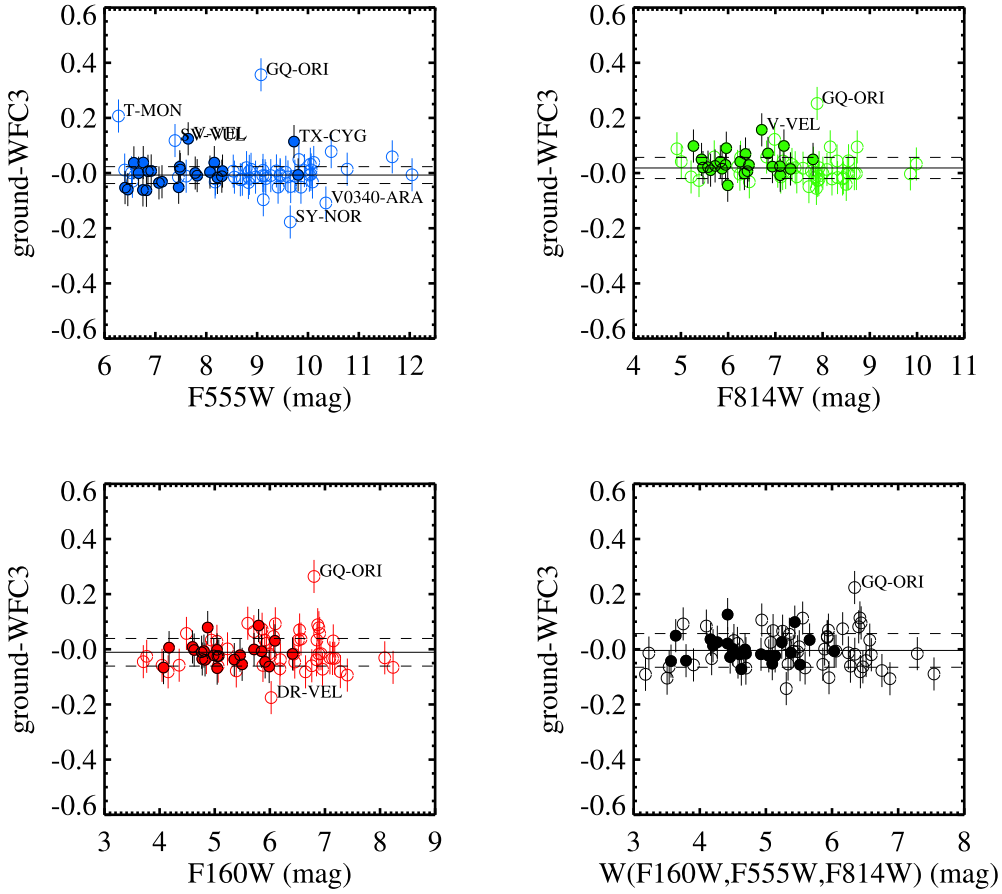

Figure 1. Comparison of Cepheid mean magnitudes in three HST WFC3 bands for observations obtained with HST and from the ground (transformed to the HST system). Filled circles are from the new Cycle 27 sample, open are from Cycle 22 and R18b.

HST Cepheid photometry and that in Groenewegen (2018). After identifying a few indicated outliers (assuming fixed errors from the ground catalogs) we derive new transformations of:

$$F555W = V + 0.202(J-H) + 0.060$$
$$F814W = V - 0.480(J-H) - 0.025$$
$$F160W = H + 0.257(J-H) - 0.022$$

with dispersions of 0.031, 0.039, and 0.050 mag, respectively, between the HST and ground-transformed magnitudes. These transformations agree to within 0.01 mag of those given in Breuval et al. (2020) based on the data in R18b. We note that the mean $J-H$ color of the Cepheids is 0.43 mag, so there is a substantial zero-point difference between H and F160W of ~0.08 mag. The ground-to-HST transformation for F160W includes precorrecting the HST magnitudes for count-rate nonlinearity (hereafter, CRNL) between their fluxes and the brightness of the standard star P330E, a mean correction of 0.017 mag. This ensures the agreement of ground and HST photometry where the HST zero-points are defined.[7]

Although there are several hundred MW Cepheids observed from the ground for which these transformations can be used, the great value of this sample of 75 is in their photometric consistency. By measuring all Cepheids along the distance ladder (and in both hemispheres) with a single, stable photometric system (HST/WFC3) we can largely eliminate the propagation of zero-point and bandpass uncertainties among Cepheid flux measurements. As discussed in Section 3.2, the lower precision per object means that the weight of the remaining ground sample with good EDR3 parallaxes provides only modest gains.

These 75 m_H^W values have a mean uncertainty of 0.021 mag, including photometric measurement errors, phase corrections, and error propagation to the Wesenheit index, corresponding to approximately 1% in distance; at the mean expected parallax of 400 μas this represents a mean uncertainty of 4 μas in the predicted parallax. At this level of precision, both the breadth of the instability strip at 0.04–0.08 mag in m_H^W as seen by Persson et al. (2004), Macri et al. (2015), and Riess et al. (2019, hereafter R19), and the expected parallax uncertainties by the end of the Gaia mission (5–14 μas) will still dominate the determination of individual Cepheid luminosities. Some of these Cepheids have been suggested as possible binaries; in general, we do not automatically exclude such objects from consideration, rather we use the Gaia goodness of fit parameter to indicate whether their parallaxes have been compromised by an astrometric binary.

In Table 1 we provide the photometric measurements[8] of these 75 Cepheids for WFC3 F555W, F814W, F160W, and m_H^W. We also include individual metallicity measurements as

[7] The use of ground-based NIR magnitudes with these transformations still requires the addition of 0.030 mag to account for the CRNL that applies to the faint extragalactic Cepheids with HST photometry in R16.

[8] m_H^W measurements include a WFC3-IR CRNL correction to account for the 6.4 dex flux ratio in F160W between these MW Cepheids and the sky-dominated extragalactic Cepheids (R18b).

Table 1
Photometric Data for MW Cepheids

Cepheid	log P	F555W	σ	F814W	σ	F160W[a]	σ	m_H^{W}[b]	σ	[Fe/H][c]	π_{R16}[d]	σ	π_{EDR3}[e]	σ
Cycle 22 set														
AA-GEM	1.053	9.9130	0.029	8.542	0.025	7.348	0.017	6.860	0.023	−0.080	0.259	0.008	0.311	0.019
AD-PUP	1.133	10.015	0.028	8.675	0.023	7.488	0.020	7.011	0.024	−0.060	0.214	0.006	0.254	0.018
AQ-CAR	0.990	8.9836	0.020	7.854	0.009	6.766	0.007	6.373	0.011	0.013	0.354	0.010	0.361	0.017
AQ-PUP	1.479	8.8671	0.018	7.120	0.014	5.487	0.013	4.859	0.016	0.060	0.340	0.010	0.294	0.025
BK-AUR	0.903	9.5609	0.036	8.220	0.038	7.015	0.021	6.539	0.029	0.070	0.371	0.011	0.426	0.016
BN-PUP	1.136	10.051	0.033	8.505	0.017	7.198	0.015	6.642	0.021	0.030	0.251	0.007	0.301	0.016
CD-CYG	1.232	9.1207	0.011	7.468	0.012	5.900	0.012	5.307	0.014	0.120	0.398	0.011	0.394	0.018
CP-CEP	1.252	10.757	0.015	8.638	0.052	6.871	0.022	6.095	0.030	0.050	0.270	0.008	0.279	0.022
CR-CAR	0.989	11.750	0.019	9.973	0.018	8.384	0.014	7.736	0.017	−0.080	0.190	0.005	0.194	0.016
CY-AUR[f]	1.141	12.052	0.012	9.953	0.020	8.106	0.025	7.334	0.027	−0.150	0.183	0.006	…	…
DD-CAS	0.992	10.036	0.007	8.523	0.011	7.108	0.012	6.566	0.013	0.160	0.319	0.009	0.346	0.014
DL-CAS[f]	0.903	9.1059	0.019	7.569	0.022	6.238	0.018	5.689	0.021	0.050	0.550	0.016	…	…
DR-VEL	1.049	9.7083	0.034	7.770	0.020	6.183	0.021	5.479	0.026	0.024	0.488	0.015	0.520	0.015
GQ-ORI	0.935	8.7199	0.020	7.632	0.024	6.523	0.032	6.146	0.034	0.250	0.418	0.013	0.408	0.023
HW-CAR	0.964	9.2782	0.016	8.007	0.013	6.798	0.005	6.350	0.009	0.060	0.370	0.010	0.397	0.013
KK-CEN	1.086	11.598	0.017	9.862	0.021	8.292	0.015	7.660	0.018	0.210	0.167	0.005	0.152	0.017
KN-CEN	1.532	10.062	0.023	7.924	0.017	5.856	0.006	5.076	0.013	0.550	0.273	0.008	0.251	0.020
RW-CAM[f]	1.215	8.8673	0.015	7.044	0.014	5.451	0.021	4.794	0.022	0.080	0.519	0.015	…	…
RW-CAS	1.170	9.3719	0.021	7.863	0.016	6.483	0.022	5.944	0.024	0.280	0.322	0.010	0.334	0.021
RY-CAS	1.084	10.075	0.019	8.333	0.040	6.715	0.010	6.085	0.020	0.320	0.342	0.010	0.359	0.016
RY-SCO	1.308	8.2067	0.012	6.206	0.010	4.408	0.010	3.685	0.012	0.010	0.757	0.021	0.764	0.035
RY-VEL	1.449	8.5234	0.036	6.757	0.016	5.211	0.017	4.576	0.023	0.090	0.403	0.012	0.376	0.023
S-NOR	0.989	6.5779	0.011	5.410	0.012	4.391	0.012	3.990	0.014	0.100	1.054	0.030	1.099	0.024
S-VUL[g]	1.839	9.1668	0.008	6.862	0.012	4.885	0.010	4.043	0.011	0.090	0.287	0.008	0.237	0.022
SS-CMA	1.092	10.121	0.012	8.444	0.008	6.894	0.011	6.289	0.012	0.012	0.315	0.009	0.308	0.014
SV-PER[f]	1.046	9.2186	0.016	7.760	0.014	6.435	0.027	5.916	0.028	0.030	0.400	0.012	…	…
SV-VEL	1.149	8.7316	0.026	7.302	0.009	6.024	0.010	5.517	0.015	0.090	0.411	0.012	0.434	0.019
SV-VUL[g]	1.653	7.2675	0.047	5.648	0.033	4.214	0.027	3.639	0.035	0.110	0.457	0.015	0.402	0.023
SY-NOR[f]	1.102	9.8284	0.023	7.925	0.038	6.214	0.013	5.523	0.022	0.230	0.435	0.013	…	…
SZ-CYG	1.179	9.6209	0.013	7.756	0.017	6.004	0.008	5.329	0.012	0.150	0.426	0.012	0.445	0.014
T-MON	1.432	6.0680	0.023	4.828	0.016	3.725	0.021	3.298	0.024	0.040	0.749	0.022	0.745	0.057
U-CAR	1.589	6.3852	0.038	4.967	0.023	3.768	0.019	3.272	0.026	0.250	0.589	0.018	0.561	0.025
UU-MUS	1.066	9.9212	0.024	8.457	0.025	7.108	0.010	6.584	0.017	0.190	0.282	0.008	0.306	0.013
V-339-CEN	0.976	8.8402	0.024	7.321	0.016	5.990	0.024	5.448	0.026	−0.080	0.557	0.017	0.568	0.023
V-340-ARA	1.318	10.460	0.024	8.554	0.014	6.808	0.012	6.115	0.016	−0.080	0.245	0.007	0.239	0.022
VW-CEN	1.177	10.379	0.031	8.718	0.023	7.158	0.010	6.558	0.018	0.410	0.238	0.007	0.260	0.017
VX-PER	1.037	9.4589	0.008	7.906	0.006	6.470	0.009	5.914	0.010	0.030	0.407	0.011	0.392	0.019
VY-CAR	1.276	7.6162	0.014	6.253	0.007	4.991	0.004	4.513	0.007	0.080	0.539	0.015	0.565	0.018
VZ-PUP	1.365	9.7715	0.033	8.262	0.022	6.931	0.017	6.390	0.023	−0.010	0.200	0.006	0.220	0.016
WX-PUP	0.951	9.1909	0.030	7.944	0.012	6.807	0.010	6.368	0.016	−0.010	0.376	0.011	0.387	0.017
WZ-SGR	1.339	8.2021	0.012	6.481	0.013	4.858	0.009	4.242	0.011	0.280	0.547	0.015	0.612	0.031
X-CYG	1.214	6.5295	0.020	5.230	0.049	4.080	0.033	3.629	0.039	0.160	0.883	0.029	0.910	0.022
X-PUP	1.414	8.6949	0.019	7.128	0.010	5.628	0.008	5.069	0.012	0.020	0.341	0.010	0.397	0.022
XX-CAR	1.196	9.4627	0.027	8.067	0.015	6.833	0.022	6.337	0.025	0.010	0.264	0.008	0.305	0.016
XY-CAR	1.095	9.4660	0.011	7.927	0.009	6.455	0.006	5.904	0.008	0.012	0.375	0.010	0.390	0.015
XZ-CAR	1.221	8.7725	0.017	7.217	0.006	5.770	0.007	5.215	0.010	0.026	0.425	0.012	0.473	0.020
YZ-CAR	1.259	8.8644	0.016	7.401	0.007	5.991	0.013	5.471	0.015	−0.030	0.359	0.010	0.358	0.020
YZ-SGR	0.980	7.4662	0.021	6.176	0.014	5.103	0.020	4.653	0.022	0.120	0.786	0.023	0.860	0.027
Z-LAC	1.037	8.5686	0.022	7.157	0.015	5.917	0.018	5.417	0.021	0.070	0.509	0.015	0.510	0.023
Cycle 27 set														
AG-CRU	0.584	8.3175	0.013	7.307	0.011	6.414	0.027	6.068	0.028	0.020	0.748	0.023	0.758	0.022
AP-PUP	0.706	7.4560	0.016	6.412	0.014	5.534	0.027	5.177	0.028	−0.020	0.941	0.029	0.924	0.022
AP-SGR	0.704	7.1056	0.028	6.036	0.013	5.094	0.027	4.729	0.030	0.160	1.145	0.035	1.217	0.026
BF-OPH	0.609	7.5091	0.018	6.347	0.010	5.374	0.027	4.972	0.028	0.110	1.184	0.036	1.189	0.026
BG-VEL	0.840	7.7827	0.010	6.299	0.009	5.054	0.019	4.529	0.020	0.040	1.033	0.030	1.045	0.019
ER-CAR	0.888	6.9095	0.011	5.916	0.012	5.078	0.027	4.742	0.028	0.120	0.867	0.026	0.869	0.016
R-CRU	0.765	6.8479	0.017	5.856	0.016	4.984	0.027	4.649	0.028	0.100	1.088	0.033	1.078	0.031
R-MUS	0.876	6.4568	0.009	5.447	0.008	4.609	0.019	4.268	0.020	−0.110	1.117	0.033	1.076	0.019
R-TRA	0.530	6.7236	0.013	5.794	0.014	5.025	0.019	4.714	0.020	0.160	1.497	0.044	1.560	0.018
RV-SCO	0.783	7.1616	0.010	5.871	0.007	4.773	0.019	4.323	0.020	0.080	1.234	0.036	1.257	0.023
RX-CAM[f]	0.898	7.8310	0.016	6.215	0.013	4.791	0.028	4.216	0.029	0.080	1.090	0.034	…	…

Table 1
(Continued)

Cepheid	log P	F555W	σ	F814W	σ	F160W[a]	σ	m_H^{W}[b]	σ	[Fe/H][c]	π_{R16}[d]	σ	π_{EDR3}[e]	σ
RY-CMA	0.670	8.2358	0.015	7.111	0.013	6.045	0.027	5.656	0.028	0.140	0.787	0.024	0.825	0.032
S-CRU[h]	0.671	6.6700	0.050	5.698	0.011	4.843	0.027	4.516	0.033	0.080	1.335	0.042	1.342	0.026
S-TRA	0.801	6.5171	0.013	5.553	0.012	4.752	0.027	4.429	0.028	0.010	1.150	0.035	1.120	0.024
SS-SCT	0.565	8.3122	0.010	7.073	0.005	6.034	0.019	5.600	0.019	0.110	0.948	0.028	0.934	0.025
T-VEL	0.667	8.1205	0.009	6.915	0.007	5.839	0.019	5.419	0.020	−0.160	0.904	0.026	0.940	0.018
TX-CYG	1.168	9.6108	0.024	7.083	0.015	4.789	0.027	3.862	0.029	0.260	0.844	0.026	0.829	0.020
U-AQL[f]	0.847	6.5396	0.019	5.168	0.029	4.115	0.027	3.636	0.030	0.140	1.531	0.047	⋯	⋯
U-SGR	0.829	6.8864	0.018	5.388	0.011	4.143	0.027	3.615	0.028	0.140	1.588	0.049	1.605	0.025
V-CAR	0.826	7.4753	0.009	6.403	0.008	5.463	0.019	5.096	0.020	0.080	0.810	0.024	0.797	0.015
V-VEL	0.641	7.5198	0.013	6.555	0.010	5.693	0.027	5.366	0.028	0	0.951	0.029	0.953	0.019
V0386-CYG	0.721	9.8126	0.015	7.748	0.014	5.944	0.027	5.192	0.028	0.170	0.901	0.028	0.894	0.014
V0482-SCO	0.656	8.0697	0.013	6.773	0.013	5.697	0.027	5.242	0.028	0.019	0.982	0.030	0.993	0.028
V0636-SCO	0.832	6.8167	0.009	5.618	0.008	4.568	0.020	4.154	0.021	0.070	1.239	0.036	1.180	0.037
W-GEM	0.898	7.0841	0.057	5.899	0.018	4.863	0.027	4.454	0.036	−0.010	0.984	0.032	1.006	0.031

Notes.
[a] Does not include addition of 0.0075 ± 0.006 mag dex^{-1} to correct CRNL for 5–6.5 dex between MW and extragalactic Cepheids.
[b] Includes addition of CRNL to allow direct comparison to extragalactic Cepheids in R16, which lack any CRNL correction.
[c] From Groenewegen (2018).
[d] $\pi_{\rm phot} = 10^{-0.2(\mu-10)}$ where $\mu = m_H^W - M_H^W$, and M_H^W is the absolute Wesenheit magnitude determined from the Cepheid period and the distance scale from Riess et al. (2016) where $b_W = -3.26$, $Z_W = -0.17$ mag dex^{-1}, $M_{H,1}^W = -5.93$ mag, which results in $H_0 = 73.24$km s^{-1} Mpc^{-1} as discussed in the text.
[e] Includes L20b parallax offset, does not include addition of best-fit residual parallax offset found here, -14μas. EDR3 errors increased by 10%.
[f] Unreliable EDR3 parallax, see the text.
[g] Possible outlier, see the text.
[h] S Cru in F555W transformed from v in Groenewegen (2018) due to HST failed acquisition.

compiled by Groenewegen (2018) for use in the Cepheid P–L relation, which span a range of −0.16 to +0.55 dex.

3. Gaia EDR3

Gaia EDR3 (Gaia Collaboration et al. 2020) contains full astrometric single-source solutions and three-band photometry, including their open-filter G magnitude and two-color photometry in the integrated G_{BP} and G_{RP}, for nearly 1.5 billion sources. The quality of the parallaxes of MW Cepheids has markedly improved from Gaia DR2 to EDR3, as we will see in the next section. The improvements result from an increase in the sampling (34 versus 22 months), improved analysis of the data (Lindegren et al. 2020a, 2020b, hereafter L20a, b), and an improved characterization of the leading systematic uncertainty in DR2: the parallax offset term.

The calibration model used in EDR3 is also far more extensive, and includes several additional parameters motivated by trends seen in preliminary solutions (Section 3.3 of L20a). In addition, the EDR3 solution makes extensive use of color information for each source in order to remove chromaticity effects, especially color-dependent offsets in the PSF position in the Gaia focal place (see Section 2.3 of L20a). The use of color information in EDR3 comes in two different flavors. The standard solution, obtained for a majority of the sources, uses the effective wavenumber $\nu_{\rm eff}$ calculated from the sampled and calibrated spectra in the blue and red photometers, to estimate chromaticity effects in the PSF; these are described as five-parameter solutions and are identified in the EDR3 catalog by having `astrometric_params_solved`=31. However, about 12% of the sources brighter than $G = 18$ (and two-thirds overall) lack a valid $\nu_{\rm eff}$ for various reasons; for these, the astrometric data themselves were used to estimate the chromatic shift of the PSF in each observation. The resulting solution has six parameters: the five standard astrometric parameters and a "pseudocolor," i.e., a color estimate that minimizes the residuals in the astrometric solution. Such solutions are identified in the EDR3 catalog by having `astrometric_params_solved` = 95. Most of the 75 Cepheid parallaxes used in this work come from the five-parameter EDR3 solution, with 12 coming from the six-parameter solution.

The parallax offset has been studied very carefully for EDR3 (L20b). The authors have used a combination of quasar, LMC stars, and physically bound pairs to constrain the parallax offset and its variation over a broad range of magnitude, color, and ecliptic latitude. The parallax for all quasars is assumed to be zero; the parallax for all LMC stars is assumed to be the same, but no assumption is made on its value. For stars in physical pairs, the assumption is that both elements have the same parallax. On the basis of these data, the authors obtained an approximate expression for the mean parallax offset as a function of magnitude G, color, and ecliptic latitude.

We use the formulation of L20b to initially calibrate the parallax offsets. Our HST sample of 75 MW Cepheids occupies a modest range of color space as expected for stars with F-K spectral types: median $\nu_{\rm eff}$ of 1.42 μm^{-1} with a dispersion of 0.055 μm^{-1} and a full range of 1.30–1.53 μm^{-1}, corresponding to a median F555W−F814W of 1.46 mag and a full range of 0.93–2.53 mag. The median G is 8.3 mag with a dispersion of 1.3 mag and a full range of 6.1–11.2 mag. The Cepheids are well distributed in ecliptic latitude, $-72° < \beta < +62°$. Among the three properties that determine the EDR3 parallax offset following the L20b prescription, ecliptic latitude dominates the variation in this value for our sample, as shown in Figure 2. The dependence follows a parabolic function of β, reaching a minimum of -38 μas near $\beta = 0$ and increasing to -20 μas at $|\beta| \approx 50°$. The median parallax offset for the Cepheid sample is -24 μas with a dispersion of 9 μas and a full range of -38 to

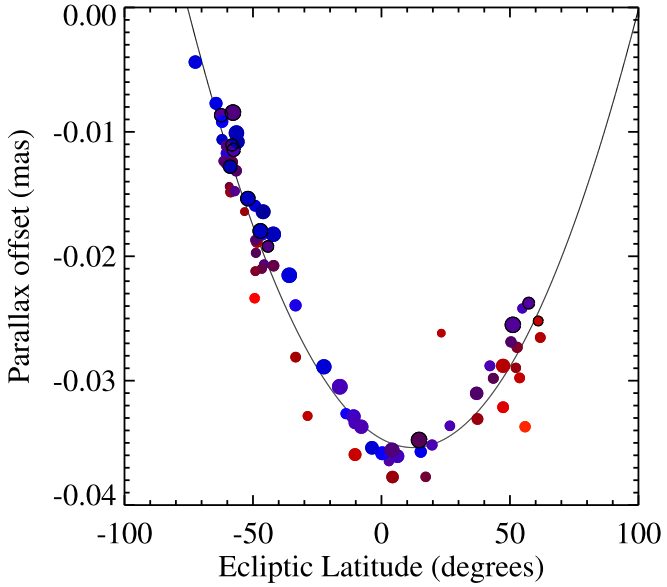

Figure 2. Parallax offsets from the L20b formulae. The primary dependence of the parallax offset is a parabolic dependence on ecliptic latitude. There is a small variation with G magnitude (indicated by the size of the point) and color (indicated by the color of the point). The Cepheid CY Aur sits about 10 μas above the parabola and its excluded from the analysis due to an uncertain parallax offset. Circles with black outline have six-parameter solutions in Gaia EDR3.

-4 μas. The dispersion perpendicular to the parabolic dependence on β drops to 1.8 μas. One Cepheid (CY Aur, the faintest in our sample) diverges from the β dependence. Its mean magnitude is near a sharp inflection point in the L20b formulae at $G = 11$ mag, where the parallax offset changes from -43 to -24 μas between $G = 10.8$ and 11.2 mag. Given this large range of offset values and since the brightness of CY Aur may vary across this boundary, we will cautiously treat its parallax as unreliable.

It is reasonable to expect some residual uncertainty in the parallax offset for these Cepheids because their magnitude range does not overlap with either the quasars or LMC stars as further discussed in Section 4. L20b suggests an uncertainty of "a few microarcseconds" in the parallax offset across the well-calibrated range. Because our Cepheids are at the bright end of this range, we will adopt a somewhat more conservative a priori global uncertainty of 10 μas for the L20b parallax offset. The P–L relation itself provides a strong tool to refine the offset in this range, as we will show in the following.

Not all Cepheids can be expected to yield useful parallaxes from EDR3. The most likely reason for a bad parallax is binarity with a period close to one year or a close association with a PSF that blends with the Cepheid. Groenewegen (2018) found Cepheids with a high value of the Gaia parameter `astrometric_gof_al`, which is calculated using the renormalized unit weight error (RUWE) per the Gaia DR3 data model, usefully identified compromised Cepheid parallaxes. Two of our Cepheids, RW Cam and SV Per, have `astrometric_gof_al` > 100 and were seen by R18b with HST imaging to have companions blended within 0.″2. There are four others with high `astrometric_gof_al` of 18 to 28, all in known binaries: U Aql (Gallenne et al. 2019), DL Cas (Evans 1995), SY Nor (Kervella et al. 2019), and AD Pup (Szabados et al. 2013). The rest of the sample has `astrometric_gof_al` values of 12.5 or lower with no major gaps, so we set this as the threshold for inclusion and will later check for outliers. (We note these six Cepheids with `astrometric_gof_al` > 12.5 also have 6 of the 7 highest values of RUWE, all >1.55.) This leaves us with 68 Cepheids, as indicated in Table 1.

3.1. Photometric and Astrometric Parallaxes

We compare the EDR3 Cepheid parallaxes to their photometrically predicted values using the Cepheid P–L relation used to measure H_0 (R16). It is advantageous to work in "parallax space" to retain the Gaussian description of the Gaia EDR3 parallax errors.

From the definition of the Wesenheit index in Equation (1), the photometric distance modulus of a Cepheid is given by the difference in magnitudes of an apparent and absolute flux, $\mu_0 = m_H^W - M_H^W$. This is expressed following the P–L relation in R16 for the ith Cepheid as

$$\mu_{0,i} = m_{i,H}^W - (M_{H,1}^W + b_W\,(\log P_i - 1) + Z_W\,\Delta[\mathrm{O/H}]_i), \quad (2)$$

where $M_{H,1}^W$ is the absolute magnitude[9] for a Cepheid with $\log P = 1$ ($P = 10$ days) and solar metallicity, while b_W and Z_W define the relation between Cepheid period, metallicity, and luminosity. The apparent magnitude, m_H^W, is given in Equation (1). The distance modulus is $\mu_0 = 5 \log D + 25$, with D being the luminosity distance in Mpc. We use the abundance values of [Fe/H] (Table 1) to set the values of Δ[O/H] in Equation (2).

The expected parallax, $\pi_{\mathrm{phot,i}}$ in units of mas, is given by

$$\pi_{\mathrm{phot,i}} = 10^{-0.2(\mu_{0,i}-10)}. \quad (3)$$

With negligible uncertainties in the periods, the mean uncertainties in the predicted parallaxes are 1% in distance from the photometric measurements of the previous section and $\sim$2%–3% in distance due to the width of the instability strip. Because the photometry uncertainties are very small, they are very close to symmetric in parallax or distance, to better than a tenth of a percent.

In Figure 3 we compare the parallaxes using the values of $b_W = -3.26$, $M_{H,1}^W = -5.93$ mag, and $Z_W = -0.17$ mag dex^{-1} from R19. With no free parameters and no additional characterization of the parallax offset, the agreement between parallaxes appears quite good. The improvement from the comparable result with DR2 and the smaller HST sample from R18b, also shown in Figure 3, is striking. The improved precision of the parallaxes is evident and most easily seen at lower-parallax values where the HST sample is unchanged.

Closer scrutiny of the residuals indicates a modest over-correction of the parallax offset, with a median difference of 15 μas (formally significant at $\sim 3\sigma$) and no visible correlation at the 1σ level with parallax, either measured or predicted (which, if present, would indicate a distance scale term). There are also two Cepheids (S Vul and SV Vul) near the boundary of Chauvenet's outlier criterion for a sample of this size ($\sim 2.6\sigma$); we tentatively exclude these two objects, but we will give our final results with and without them. We also show in Figure 3 the predictions of the Cepheid parallaxes for a range of values of H_0.

[9] $M_{H,1}^W$ was defined at $P = 1$ day in R16, and was changed here to $\log P = 1$ ($P = 10$ days) for consistency with Breuval et al. (2020).

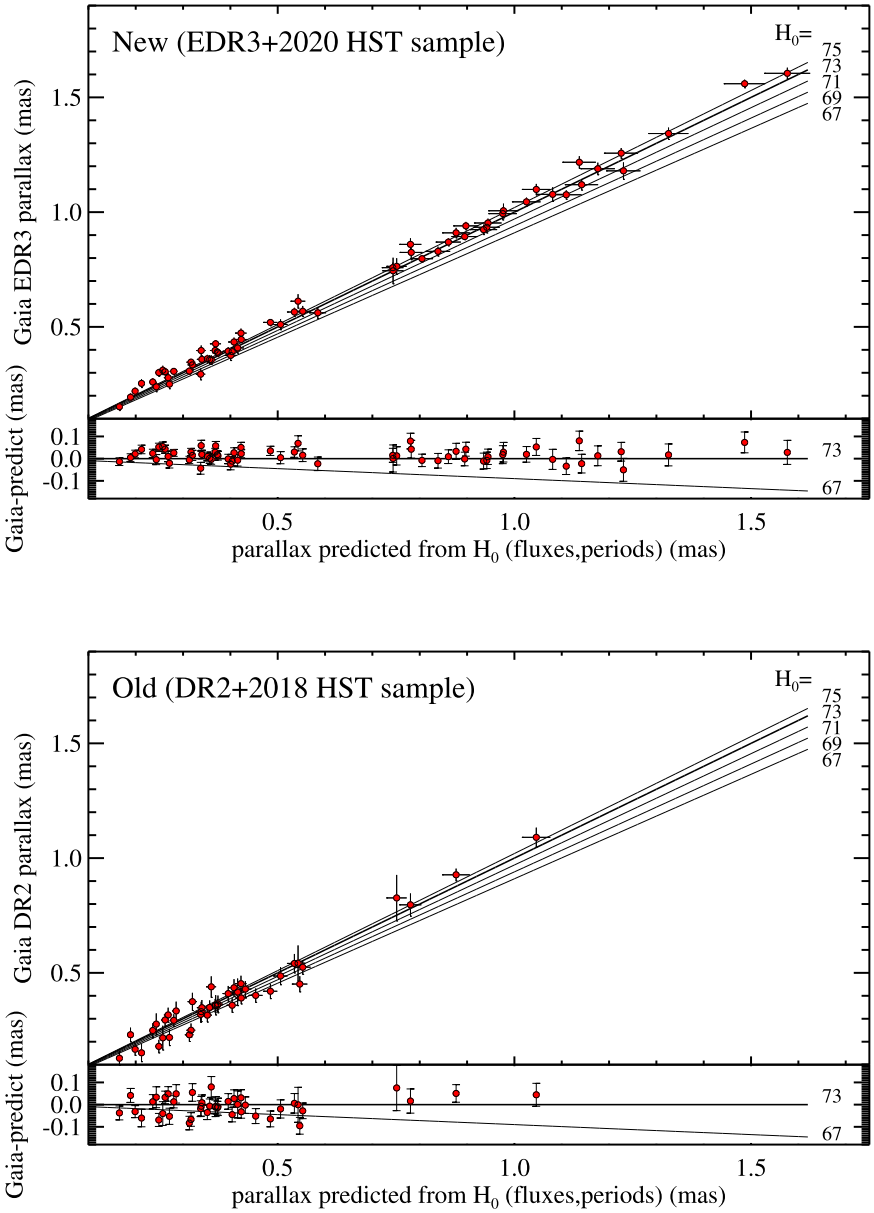

Figure 3. Comparison of Milky Way Cepheid parallaxes provided in Gaia EDR3 for the present expanded sample (left) and DR2 for the earlier, smaller sample available in Riess et al. (2018b; right) vs. photometric parallaxes using the HSTWFC3-based photometry in Table 1, the Cepheid periods, and the P–L parameters given by R16 and R19.

Our goal, as in R18b, is to simultaneously determine two parameters: the optimal parallax offset applicable to bright Cepheids, an additive term to parallax, and the calibration of the distance scale, a multiplicative term of parallax. However, rather than assuming the other parameters, which characterize the P–L relations of MW and extragalactic Cepheids as being the same, we first undertake a more general four-parameter analysis including the slope b_W and metallicity term Z_W defined above, to determine their consistency.

Therefore we seek to optimize the value of:

$$\chi^2 = \sum \frac{(\pi_{\mathrm{EDR3},i} - \pi_{\mathrm{phot},i} + zp)^2}{\sigma_i^2}, \quad (4)$$

where zp is a residual parallax offset after application of the L20b-derived parallax offset and $\pi_{\mathrm{phot,i}}$ is a function of the Cepheid P–L parameters b_W, $M^W_{H,1}$, Z_W (as given in Equations (2) and (3)). Note that these parameters are separable as zp is additive to the photometric parallaxes, $M^W_{H,1}$ is multiplicative, and b_W, Z_W depend on individual periods and metallicities.

We determine the individual σ_i by adding in quadrature the photometric parallax uncertainty, the intrinsic width of the NIR Wesenheit P–L (0.06 mag), and the parallax uncertainty given in the EDR3 release. Based on some suggestions of possible excess uncertainty in the Gaia EDR3 data validation (see Figure 21 of Fabricius et al. 2020), we conservatively increase the nominal parallax uncertainty assigned in the EDR3 release by 10% (an augmentation of 30% was indicated for the prior DR2 as discussed in L18b and R18b, so excess uncertainty appears to be less for EDR3). The mean of the EDR3 uncertainties is 21 μas (median 20 μas), while the mean of the full σ_i is 29 μas (median 27 μas).

Minimizing the value of χ^2 gives values of $b_W = -3.28 \pm 0.06$ mag, $Z_W = -0.20 \pm 0.13$ mag dex^{-1}, and $zp = -14 \pm 6$ μas, with

Table 2
Best Fits to Gaia EDR3

Fit	$M^W_{H,1}$ (mag)	zp (μas)	b_W (mag dex^{-1})	Z_W (mag dex^{-1})	χ^2	H_0 (km s^{-1} Mpc^{-1})
4-parameter	-5.915 ± 0.030	-14 ± 6	-3.28 ± 0.06	-0.20 ± 0.13	68.0	(73.0 ± 1.4[a])
4-parameter with outliers	-5.930 ± 0.030	-15 ± 6	-3.34 ± 0.06	-0.18 ± 0.13	78.8	(72.5 ± 1.4[a])
2-parameter (best)	-5.915 ± 0.022	-14 ± 6	-3.26[b]	-0.17[b]	68.2	73.0 ± 1.4
2-parameter with outliers	-5.910 ± 0.022	-15 ± 6	-3.26[b]	-0.17[b]	81.2	73.2 ± 1.4
1-parameter	-5.865 ± 0.013	0[c]	-3.26[b]	-0.17[b]	74.5	74.7 ± 1.3

Notes.
[a] Cepheid luminosity not determined with same P–L parameters b_W and Z_W from R19, so not directly applicable to determine H_0.
[b] Fixed to R19 values.
[c] Assuming no residual parallax offset in Gaia EDR3.

a value of $\chi^2 = 68.0$ for 66 degrees of freedom. In Table 2 we give the results of this fit and all others. The values of b_W and Z_W found here for the MW Cepheids are found to be fully consistent with the extragalactic Cepheids in R16 and R19, though they are determined with much lower precision here. The value of $M^W_{H,1}$ is not readily applicable to other Cepheids on the distance ladder because it is not determined for the same P–L relation, i.e., one using the same values of b_W and Z_W as in R16 or R19, which we remedy below.

We now calibrate the luminosity of Cepheids along the distance ladder by adopting fixed values of $b_W = -3.26$ mag and $Z_W = -0.17$ mag dex^{-1} for the slope and the metallicity term, these are the values derived by R19 from other galaxies (i.e., the LMC, M31, NGC 4258, and 19 SN Ia hosts[10]) and again optimize the value of χ^2 for the two free parameters, zp and $M^W_{H,1}$. This is the same procedure used in R18b.

We find $zp = -14 \pm 6$ μas and $M^W_{H,1} = -5.915 \pm 0.022$ mag with $\chi^2 = 68.2$ for 66 degrees of freedom. Applied to the distance ladder from R16 and R19 to calibrate SNe Ia yields $H_0 = 73.0 \pm 1.4$ km s^{-1} Mpc^{-1}. Confidence regions for the two parameters are shown in Figure 4. Although these two parameters are correlated, the range of Cepheid parallaxes (0.2–1.5 mas) largely breaks their degeneracy to provide a calibration of the distance ladder with 1% precision, better than any other individual geometric calibration (R19). There is no evidence of a correlation of the residuals with G mag (0.4σ), color (1.0σ), or ecliptic latitude (0.2σ), the three parameters used by L20b to characterize the parallax offset. We also note that the mean metallicity of the HST sample is 0.09 dex (Groenewegen 2018), slightly greater than solar, and with the empirical metallicity term, these MW Cepheids are expected to be 0.015 mag brighter on average than the definition of $M^W_{H,1}$. Including the two marginal outliers discussed in the prior section (S Vul and SV Vul) yields $zp = -15 \pm 6$ μas and $M^W_{H,1} = -5.910 \pm 0.022$ mag with $\chi^2 = 81.2$, similar parameters but with the expected higher χ^2 for 68 degrees of freedom.

If we do not include freedom for zp but rather adopt the exact L20b offsets, we find $M^W_{H,1} = -5.865 \pm 0.013$ mag and $H_0 = 74.7 \pm 1.3$ km s^{-1} Mpc^{-1}, implying a calibration with 0.6% precision. However, this solution has a significantly greater $\chi^2 = 74.5$ and ignores the strong evidence for a residual parallax offset, detected here at $\sim 2.5\sigma$ with the assumed 10 μas uncertainty in the fiducial L20b parallax offset, or more realistically 3σ (-17 ± 6 μas) with no prior on the quality of the L20b offset.

The size and direction of a residual parallax offset is also corroborated by the analysis of red giants with asteroseismic data from Kepler (Zinn et al. 2019). Zinn (2021) finds an approximate residual parallax offset of -15 ± 5 μas (same sense of an overall smaller parallax offset as found here) for brighter red giants in the range of $G = 10$–11 mag[11] and colors similar to our Cepheids. If we use this as a prior, rather than the nominal 10 μas uncertainty on the L20b offset, we find a tighter constraint of $M^W_{H,1}$ to -5.925 ± 0.018 mag, a remarkable 0.85% foundation for determining H_0 that points to the room for improvement with Gaia DR4. In the following, we conservatively adopt the nominally less precise calibration internal to the Cepheids, which effectively marginalizes over the uncertainty in the parallax offset, and without the red giant prior. Future characterization of the EDR3 parallax offset may further justify the use of a tighter constraint.

The value of $M^W_{H,1}$ is quite consistent with the value of -5.93 mag from R16, indicating that the predicted parallaxes, after accounting for the offset, are in good agreement with EDR3, and further affirming the cosmic distance scale with the value of H_0 used to predict the parallaxes from R16. Alternatively, we can use the determinations of $M^W_{H,1}$ from Gaia EDR3 to determine the distance to the LMC from its Cepheids observed with HST in R19, which yields $\mu_0 = 18.511 \pm 0.024$ for the two-parameter solution or $\mu_0 = 18.461 \pm 0.016$ for the one-parameter solution, both in good agreement with the value of $\mu_0 = 18.477 \pm 0.026$ measured from its detached eclipsing binaries (Pietrzyński et al. 2019). On the other hand, this value of $M^W_{H,1}$ is inconsistent with the value of -6.12 mag, needed to match the Planck CMB $+\Lambda$CDM value of H_0, at the 4.2σ confidence level (99.997% likelihood), confirming again the "H_0 tension" (see Verde et al. 2019 for a review).

3.2. Ground-based Sample, Caveats

We might improve the constraint on zp and $M^W_{H,1}$ (or even b_W and Z_W) by considering a larger sample of MW Cepheids, though the augmentation of the sample would need to rely exclusively on ground-based photometry. Using the Groenewegen (2018) catalog of V, J, H, K photometry and the

[10] Future analyses would ideally optimize the value of b_W and Z_W across all Cepheid hosts, but there is little difference in practice, as these parameters are far better determined from the aforementioned extragalactic samples of R16 and R19.

[11] Zinn (2021) finds good agreement with the parallax offset of L20b for red giants fainter than $G = 11$.

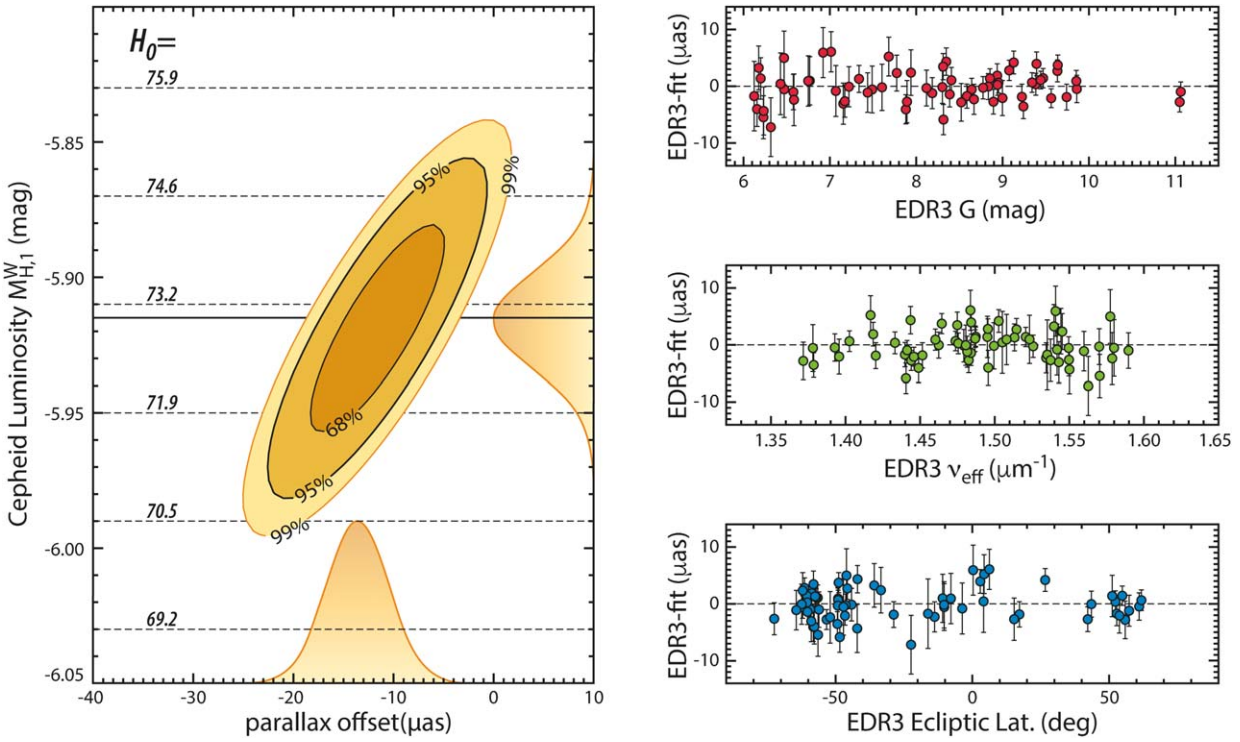

Figure 4. For the HST sample of Milky Way Cepheids, we determined the best match between the measured Gaia EDR3 parallaxes and those predicted photometrically from their photometry, periods, and the fiducial Cepheid luminosity, $M^W_{H,1}$. We allow two free parameters, an additive term to parallax to account for the parallax offset, z_p, and a multiplicative term to predicted parallax that measures the fiducial Cepheid luminosity. The Cepheid luminosity calibrates the SH0ES distance ladder from R16 and R19 and results in the indicated values of H_0. Right, top to bottom, residuals between the best fit vs. Cepheid G mag, color, and ecliptic latitude.

photometric transformations in Section 2 for fundamental-mode Cepheids would augment the HST sample by an additional ∼200 Cepheids, which have good-quality parallaxes. However, the transformed photometric uncertainty per object increases, matching the width of the instability strip, so that the statistical significance of the additional sample only just matches the HST sample. More concerning is that the HST sample was selected to have low extinction ($A_H < 0.4$ mag for the 50 Cepheids in R18b and $A_H < 0.6$ mag for the additional 25 with larger parallaxes presented here), so the additional Cepheids are mostly highly reddened and distant, so these Cepheids may offer less precise results. Our trial analyses using the ground-based sample yielded similar parameters as for the HST sample, but with a larger dispersion, which may require additional modeling of the uncertainties. It is not clear if the additional dispersion may result from Gaia uncertainties over a different range of measurement space, inhomogeneities between ground surveys, uncertainties in larger reddenings or some combination of these. We therefore chose to focus on the better-understood and more precise HST sample.

4. Discussion

4.1. The EDR3 Parallaxes

Some limitations remain in the EDR3 solution that are worth noting as they pertain to bright Cepheids. One which could be a consideration for our targets is that the solution assumes that the color of a source is the same in all observations. This is a good approximation for most stars, but it does not fully apply to our targets, which change magnitude and color according to their phase. For most bright stars, the effective wavenumber could in principle be determined independently for the majority of the observations (or, in the case of Cepheids with known light-curve ephemeris, determined on the basis of the phase for each exposure); however, this step is not yet included in the EDR3 pipeline (Section 2.3 of L20a). In practice, the color variation of a Cepheid, about ±0.25 mag in $G_{BP} - G_{RP}$ during one cycle, will add a small amount of astrometric noise, and an even smaller amount of parallax noise. Since the parallax measurement is well averaged over all phases such noise will be statistical and well below the present statistical parallax errors.

Second, and more significant, is the parallax offset due to the variation of the basic angle discovered during Gaia commissioning (L18a). Most of the basic angle variation can be constrained as part of the astrometric solution, but as noted by Butkevich et al. (2017), a near-degeneracy remains, which manifests itself as a parallax offset error and must be calibrated using external sources as undertaken in L20b. In principle, subtracting the estimated parallax offset from the catalog parallax should remove the broad dependencies from magnitude, color, and position; as seen in our analysis this approach is largely successful, and leads to a significant improvement of the data with no trend of residuals with magnitude, color, or ecliptic latitude. However, the quasar data does not meaningfully calibrate the offset at magnitudes brighter than $G = 14$ nor the LMC data brighter than $G = 11$. To reach the magnitude range of Cepheids ($G = 6 - 10$) requires inferring the offsets of the fainter stars in physical pairs (bootstrapped via the Quasar and LMC-derived formulae) and using the brighter stars in the pairs to infer the offset at lower magnitudes. This process is repeated with even brighter pairs to extend to $G = 6$. Thus the offset for these bright Cepheids is expected to be less well constrained. It is therefore not surprising that we do find evidence of a residual offset and the need to marginalize over this term lowers the precision available to calibrate the uncertainty in the

Hubble constant from 0.6% to 1.0%, a quite important cost in the quest to determine H_0 to 1% precision. We hope with EDR4 knowledge of the offset will continue to improve.

4.2. The Status of the Hubble Constant

It is quite reasonable to expect the precision of each of the three steps in the distance ladder linking geometry, Cepheids and SN Ia to measure H_0 to be determined to better than 1% in the very near future. We expect that the geometric calibration of Cepheids will approach 0.5% precision by DR4, matching the current precision of the SN Ia Hubble diagram (Scolnic et al. 2018). With the number of high quality calibrations of SN Ia with Cepheids approaching 40, a total uncertainty in the range of 1.0%–1.3% in H_0 (depending on residual systematics) appears within reach.

We expect that Gaia EDR3 will also impact the calibration of other distance indicators. EDR3 puts the parallaxes of globular clusters, most notably ω Cen, in a useful range for the first time; as a result, the direct geometric calibration of the Tip of the Red Giant Branch (TRGB) is now within reach (Soltis et al. 2020). Three studies of ω Cen with Gaia DR2 and EDR3 all give the same result, $D = 5.24$–5.25 kpc, which gives an I-band calibration of TRB of -3.97 mag and a Hubble constant of $\sim$72 km s^{-1} Mpc^{-1} (Baumgardt et al. 2019; Capozzi & Raffelt 2020; Soltis et al. 2020; Maíz Apellániz et al. 2021), similar to Cepheids calibrated with Gaia EDR3 as presented here.

We may hope that enhanced measurements or theoretical insights will lead to an explanation of the present $\sim 5\sigma$ tension between direct determinations of the Hubble constant and values inferred from ΛCDM calibrated with Early Universe physics and the CMB (see Verde et al. 2019 for a review).

We are grateful to the entire Gaia collaboration for providing data and assistance that made this project possible. We congratulate them on their tremendous achievement to date. We acknowledge with thanks the variable star observations from the AAVSO International Database contributed by observers worldwide and used in this research.

Support for this work was provided by the National Aeronautics and Space Administration (NASA) through programs GO-12879, 13334, 13335, 13344, 13571, 13678, 13686, 13928, 13929, 14062, 14394, 14648, 14868, and 15879 from the Space Telescope Science Institute (STScI), which is operated by AURA, Inc., under NASA contract NAS 5-26555.

A.G.R., S.C., and L.M.M. gratefully acknowledge support by the Munich Institute for Astro- and Particle Physics (MIAPP) of the DFG cluster of excellence "Origin and Structure of the Universe." J.C.Z. is supported by an NSF Astronomy and Astrophysics Postdoctoral Fellowship under award AST-2001869.

The HST data used in this paper are available at the MAST archive at 10.17909/t9-2gmg-xc49.

Appendix

Listed in Tables 3 and 4 are the sources of photometry used to derived transformations from individual observation epochs to mean phase.

Table 3
Ground Data Sources

Identifier	References[a]				
	Phase Determination	V	I	J	H
AG CRU	1,22,28,29	22,28,29	22,28,29	NA	NA
AP PUP	1,28	28	28	NA	NA
AP SGR	1,3–5,7–13,22,28	3–5,7–13,22,28	11,12,22,28	NA	NA
BF OPH	1,3–7,17,22,28	3–7,22,28	22,28	NA	NA
BG VEL	1,28	28	28	NA	NA
ER CAR	25,28	28	28	NA	NA
R CRU	1,28	28	28	NA	NA
R MUS	25,28	28	28	NA	NA
R TRA	1,22,28	22,28	22,28	NA	NA
RV SCO	1,3,22,28	3,22,28	22,28	NA	NA
RX CAM	3,21,24,28	3,21,24,28	3	NA	NA
RY CMA	1,3,28	3,28	28	NA	NA
S CRU	1,22,28	22,28	22,28	NA	NA
S TRA	1,22,28	22,28	22,28	NA	NA
SS SCT	1–4,9,20,22,28	3,4,9,20,22	22	NA	NA
T CRU	1,28	28	28	NA	NA
T VEL	1,17,28	28	28	NA	NA
TT AQL	1–3,8–10,12–16,18,19,28	3,8–10,12–16,18,19,28	12,19,28	2,18	2,18
TX CYG	3,8,9,15,16,24,28	3,8,9,15,16,24,28	3	NA	NA
U AQL	1–14,28	3–14,28	30	NA	NA
U SGR	1–5,8–13,16,17,22–24,28	3–5,8–13,16,22–24,28	11,12,22,28	NA	NA
V CAR	1,17,28	28	28	NA	NA
V VEL	1,26,28	26,28	26,28	NA	NA
V386 CYG	3,21,23,28	3,21,23,28	3	NA	NA
V482 SCO	1,3,22,28	3,22,28	22,28	NA	NA
V636 SCO	25,28	28	28	NA	NA
W GEM	1,3,14,21,24,28	3,14,21,24,27,28	30	NA	NA

Note.
[a] The labels are described in Table 4. NA indicates no ground data available.

Table 4
References for the Labels in Table 3

Reference ID	Reference	Comments
1	Pel (1976)	McMaster
2	Welch et al. (1984)	McMaster
3	Moffett & Barnes (1984)	McMaster
4	Berdnikov (1992a)	McMaster
5	Berdnikov (1992b)	McMaster
6	Berdnikov (1992c)	McMaster
7	Berdnikov (1992d)	McMaster
8	Berdnikov (1992e)	McMaster
9	Berdnikov (1992f)	McMaster
10	Berdnikov (1993)	McMaster
11	Berdnikov & Turner (1995)	McMaster
12	Berdnikov & Turner (1995)	McMaster
13	Berdnikov & Vozyakova (1995)	McMaster
14	Kiss (1998)	McMaster
15	Szabados (1981)	McMaster
16	Berdnikov (1986)	McMaster
17	Laney & Stobie (1992)	McMaster
18	Barnes et al. (1997)	McMaster
19	Coulson et al. (1985)	McMaster
20	Henden (1980)	McMaster
21	Szabados (1980)	McMaster
22	Gieren (1981)	McMaster
23	Berdnikov (1987)	McMaster
24	Harris (1980)	McMaster
25	Walraven et al. (1964)	McMaster
26	Gieren (1985)	McMaster
27	Kochanek et al. (2017)	ASAS-SN
28	Berdnikov et al. (2000)	
29	Berdnikov et al. (2015)	
30	AAVSO	AAVSO

ORCID iDs

Adam G. Riess https://orcid.org/0000-0002-6124-1196
Wenlong Yuan https://orcid.org/0000-0001-9420-6525
Lucas Macri https://orcid.org/0000-0002-1775-4859
Joel C. Zinn https://orcid.org/0000-0002-7550-7151

References

Anderson, R. I., & Riess, A. G. 2018, ApJ, 861, 36
Barnes, T. G., III, Fernley, J. A., Frueh, M. L., et al. 1997, PASP, 109, 645
Baumgardt, H., Hilker, M., Sollima, A., & Bellini, A. 2019, MNRAS, 482, 5138
Berdnikov, L. N. 1986, PZ, 22, 369
Berdnikov, L. N. 1987, PZ, 22, 530
Berdnikov, L. N. 1992a, A&AT, 2, 107
Berdnikov, L. N. 1992b, A&AT, 2, 157
Berdnikov, L. N. 1992c, A&AT, 2, 1
Berdnikov, L. N. 1992d, A&AT, 2, 31
Berdnikov, L. N. 1992e, A&AT, 2, 43
Berdnikov, L. N. 1992f, SvAL, 18, 130
Berdnikov, L. N. 1993, AstL, 19, 84
Berdnikov, L. N., Dambis, A. K., & Vozyakova, O. V. 2000, A&AS, 143, 211
Berdnikov, L. N., Kniazev, A. Y., Sefako, R., et al. 2015, AstL, 41, 23
Berdnikov, L. N., & Turner, D. G. 1995, AstL, 21, 717
Berdnikov, L. N., & Vozyakova, O. V. 1995, AstL, 21, 308
Breuval, L., Kervella, P., Anderson, R. I., et al. 2020, A&A, 643, A115
Butkevich, A. G., Klioner, S. A., Lindegren, L., Hobbs, D., & van Leeuwen, F. 2017, A&A, 603, A45
Capozzi, R., & Raffelt, G. 2020, PhRvD, 102, 083007
Coulson, I. M., Caldwell, J. A. R., & Gieren, W. P. 1985, ApJS, 57, 595
Evans, N. R. 1995, ApJ, 445, 393
Fabricius, C., Luri, X., Arenou, F., et al. 2020, arXiv:2012.06242
Fitzpatrick, E. L. 1999, PASP, 111, 63
Gaia Collaboration, Brown, A. G. A., Vallenari, A., et al. 2016a, A&A, 595, A2
Gaia Collaboration, Brown, A. G. A., Vallenari, A., et al. 2018, A&A, 616, A1
Gaia Collaboration, Brown, A. G. A., Vallenari, A., et al. 2020, arXiv:2012.01533
Gaia Collaboration, Prusti, T., de Bruijne, J. H. J., et al. 2016b, A&A, 595, A1
Gallenne, A., Kervella, P., Borgniet, S., et al. 2019, A&A, 622, A164
Gieren, W. 1981, ApJS, 47, 315
Gieren, W. P. 1985, ApJ, 295, 507
Groenewegen, M. A. T. 2018, A&A, 619, A8
Harris, H. C. 1980, PhD thesis, Washington Univ.
Henden, A. A. 1980, MNRAS, 192, 621
Hoffmann, S. L., Macri, L. M., Riess, A. G., et al. 2016, ApJ, 830, 10
Kervella, P., Gallenne, A., Evans, N. R., et al. 2019, A&A, 623, A117
Kiss, L. L. 1998, MNRAS, 297, 825
Kochanek, C. S., Shappee, B. J., Stanek, K. Z., et al. 2017, PASP, 129, 104502
Laney, C. D., & Stobie, R. S. 1992, A&AS, 93, 93
Lindegren, L., Bastian, U., Biermann, M., et al. 2020a, arXiv:2012.01742
Lindegren, L., Hernandez, J., Bombrun, A., et al. 2018, A&A, 616, A2
Lindegren, L., Klioner, S. A., Hernández, J., et al. 2020b, arXiv:2012.03380
Macri, L. M., Ngeow, C.-C., Kanbur, S. M., Mahzooni, S., & Smitka, M. T. 2015, AJ, 149, 117
Madore, B. F. 1982, ApJ, 253, 575
Maíz Apellániz, J., Pantaleoni González, M., & Barbá, R. H. 2021, arXiv:2101.10206
Moffett, T. J., & Barnes, T. G., III 1984, ApJS, 55, 389
Pel, J. W. 1976, A&AS, 24, 413
Persson, S. E., Madore, B. F., Krzemiński, W., et al. 2004, AJ, 128, 2239
Pietrzyński, G., Graczyk, D., Gallenne, A., et al. 2019, Natur, 567, 200
Riess, A. G., Casertano, S., Yuan, W., et al. 2018a, ApJ, 855, 136
Riess, A. G., Casertano, S., Yuan, W., et al. 2018b, ApJ, 861, 126
Riess, A. G., Macri, L. M., Hoffmann, S. L., et al. 2016, ApJ, 826, 56
Riess, A. G., Narayan, G., & Calamida, A. 2019, Calibration of the WFC3-IR Count-rate Nonlinearity, Sub-percent Accuracy for a Factor of a Million in Flux, Tech. Rep. ISR WFC3 2019-01
Sahu, K., Gosmeyer, C. M., & Baggett, S. 2015, WFC3/UVIS Shutter Characterization, Tech. Rep. ISR WFC3-2015-12
Scolnic, D. M., Jones, D. O., Rest, A., et al. 2018, ApJ, 859, 101
Soltis, J., Casertano, S., & Riess, A. G. 2020, ApJ, in press (arXiv:2012.09196)
Szabados, L. 1980, CoKon, 76, 1
Szabados, L. 1981, CoKon, 77, 1
Szabados, L., Derekas, A., Kiss, L. L., et al. 2013, MNRAS, 430, 2018
Verde, L., Treu, T., & Riess, A. G. 2019, NatAs, 3, 891
Walraven, J. H., Tinbergen, J., & Walraven, T. 1964, BAN, 17, 520
Welch, D. L., Wieland, F., McAlary, C. W., et al. 1984, ApJS, 54, 547
Zinn, J. C. 2021, arXiv:2101.07252
Zinn, J. C., Pinsonneault, M. H., Huber, D., & Stello, D. 2019, ApJ, 878, 136